Kolmogorov-Crespi Potential For Multilayer Transition Metal Dichalcogenides: Capturing Structural Transformations In Moiré Superlattices.

Mit H. Naik, Indrajit Maity, Prabal K. Maiti, and Manish Jain*

Center for Condensed Matter Theory, Department of Physics, Indian Institute of Science, Bangalore 560012, India

E-mail: mjain@iisc.ac.in

1 Computation of normals

In the main-text, we describe the procedure to determine the surface normals for the Kolmogorov-Crespi potential. To verify that the normals are computed correctly, we displace a single sheet of MoS_2 in the out-of-plane direction by a periodic function of the form $sin(x)sin(y)$, as shown in Fig. S1 (a). The normals, $\mathbf{n}(x, y)$ can be computed for this analytical function. The distribution of $|\mathbf{n}.\hat{z}|$ is shown in S1 (b). The same distribution for the displaced MoS_2 sheet computed using our implementation is shown in Fig. S1 (c), and is in good agreement with the analytical distribution. $|\mathbf{n}.\hat{z}| = 0.994$ corresponds to a maximum deviation of the normal from $\hat{z}$ by $\sim 6°$.

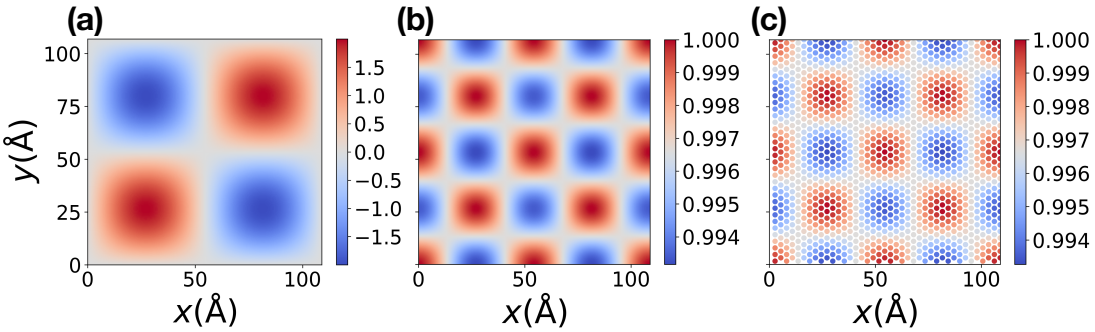

Figure S1: (a) Constructed periodic analytical function. (b) $|\mathbf{n}.\hat{z}|$ computed analytically for the distribution in (a). (c) $|\mathbf{n}.\hat{z}|$ computed using our implementation for a sheet of MoS_2 displaced in the z direction by the distribution shown in (a). The displacements are in Å.

2 Alternate parameter sets

In the main text, we propose a parameter set including M_1-X_3, M_2-X_2, X_2-X_3 and M_1-M_2 interactions. We propose two alternate approaches to capture the binding energy landcape of TMD bilayers and heterostructures. The first approach is to introduce M_1-X_3 and M_2-X_2 interactions in addition to the X_2-X_3 interaction. We denote the parameters associated with these interactions as KC^{X-X}_{M-X} (Table S1). The performance of this forcefield to capture the BE as a function of interlayer spacing and shear for bilayer systems is shown in Fig. S2.

Table S1: Parameters for KC^{X-X}_{M-X} interactions.

	z_0 (Å)	C_0 (meV)	C_2 (meV)	C_4 (meV)	C (meV)	δ (Å)	λ (Å^{-1})	A (meV)
S_2-S_3	3.751	7.273	2.715	0.069	25.900	1.063	3.045	57.990
Se_2-Se_3	4.048	8.617	6.976	0.000	29.341	1.135	2.633	66.693
Mo_1-S_3, Mo_2-S_2	4.408	-4.589	-4.304	-0.333	11.690	0.619	2.710	14.292
Mo_1-Se_3, Mo_2-Se_2	4.348	-13.745	-0.775	-0.445	34.759	0.953	2.100	19.108
W_1-S_3, W_2-S_2	5.067	-1.498	-1.423	-0.136	4.803	0.472	2.200	7.082
W_1-Se_3, W_2-Se_2	4.943	-3.868	-3.112	-0.180	9.452	0.687	2.200	7.756

The second approach is to only include X_2-X_3 and M_1-M_2 interactions. We find that this approximation is also capable of capturing the BE landscape very well. We denote these refit parameters as KC^{X-X}_{M-M} (Table S2). The performance of KC^{X-X}_{M-M} for the various bilayer systems is shown in Fig. S3. Both KC^{X-X}_{M-M} and KC^{X-X}_{M-X} can be used to simulate

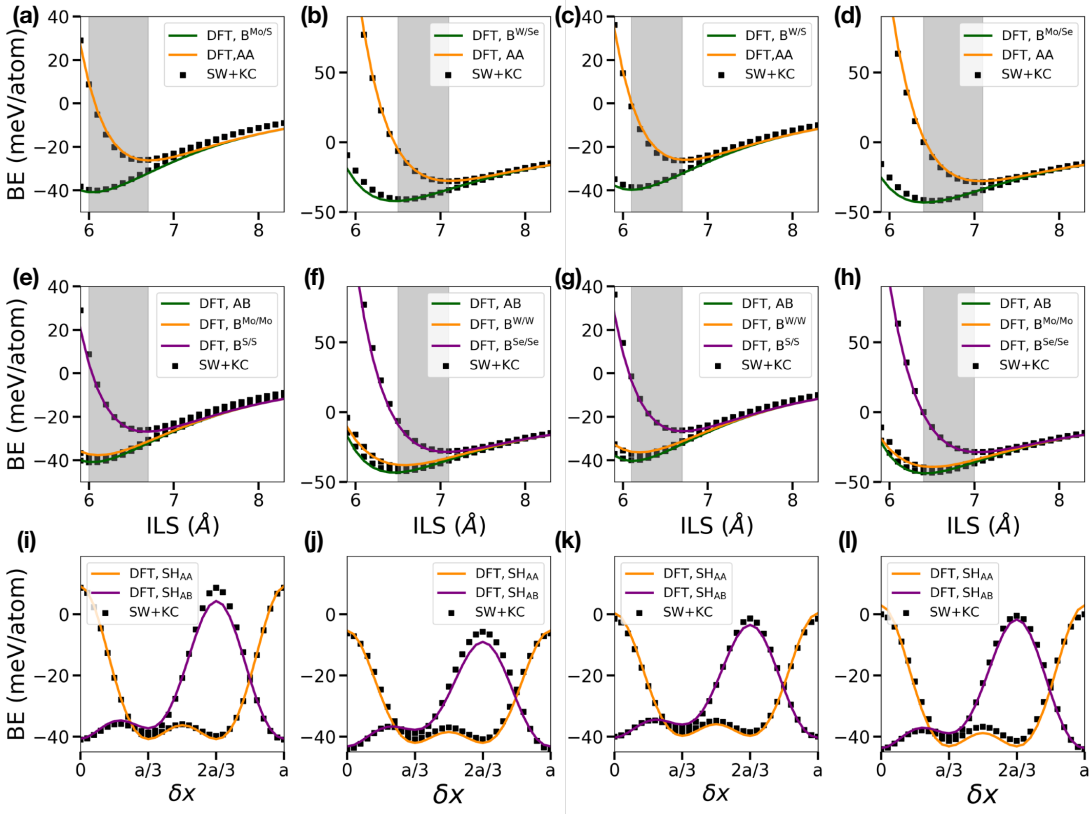

Figure S2: (a) - (h) BE computed within DFT and using SW+KC$^{\mathrm{X-X}}_{\mathrm{M-X}}$ as a function of interlayer spacing for the high-symmetry stackings in bilayer MoS_2, WSe_2, WS_2 and $MoSe_2$. The shaded region marks the range of interlayer spacings in the bilayer system. (i) - (l) BE computed within DFT and using SW+KC as a function of shear, SH_{AA} and SH_{AB}, in bilayer MoS_2, WSe_2, WS_2 and $MoSe_2$. The ILS is fixed to that of the equilibrium AB stacking.

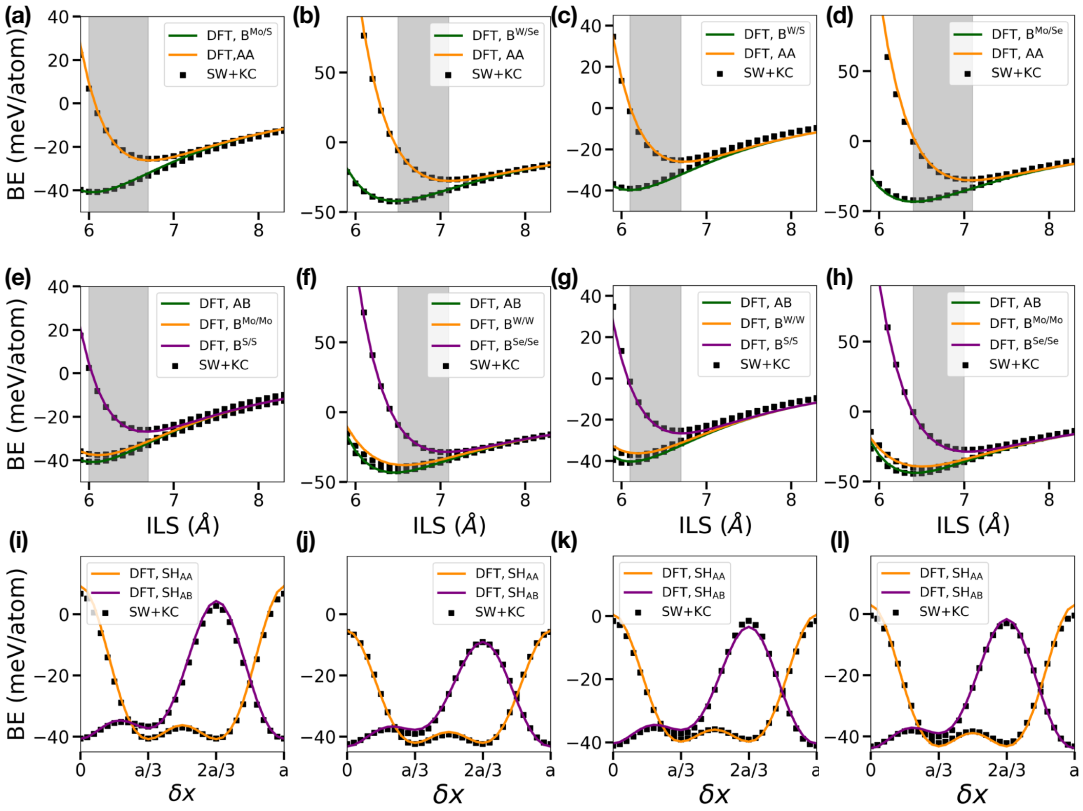

Figure S3: (a) - (h) BE computed within DFT and using SW+KC$^{\mathrm{X-X}}_{\mathrm{M-M}}$ as a function of interlayer spacing for the high-symmetry stackings in bilayer MoS_2, WSe_2, WS_2 and $MoSe_2$. The shaded region marks the range of interlayer spacings in the bilayer system. (i) - (l) BE computed within DFT and using SW+KC as a function of shear, SH_{AA} and SH_{AB}, in bilayer MoS_2, WSe_2, WS_2 and $MoSe_2$. The ILS is fixed to that of the equilibrium AB stacking.

heterostructures using the mixing rule described in the main text.

Table S2: Parameters for KC^{X-X}_{M-M} interactions.

	z_0 (Å)	C_0 (meV)	C_2 (meV)	C_4 (meV)	C (meV)	δ (Å)	λ (Å^{-1})	A (meV)
S_2-S_3	3.860	7.858	2.905	0.000	26.825	1.013	2.709	62.342
Se_2-Se_3	3.971	8.832	7.056	0.000	29.978	0.969	2.736	69.674
Mo_1-Mo_2	9.114	1.375	1.089	0.095	1.816	1.139	1.000	3.741
W_1-W_2	10.555	0.258	0.217	0.004	0.611	1.034	1.000	1.877

The lattice constants used in the DFT and forcefield calculations are provided in Table S3.

Table S3: Lattice parameters of the bilayer transition metal dichalcogenides used in our simulations.

	$BLMoS_2$	$BLWS_2$	$BLMoSe_2$	$BLWSe_2$
a (Å)	3.14	3.13	3.27	3.26

3 Twisted bilayer MoS_2

Details of the twisted bilayer MoS_2 superlattices are provided in Table S4. The MSLs are constructed using the Twister[S1] code.

Table S4: Twist angles, number of atoms and MSL vectors for the DFT calculations. In the LAMMPS calculation, the superlattice typically contains 32 repeated MSLs.

Twist Angle (θ)	No. of atoms	MSL vectors (Å)
3.5°	1626	51.8
7.3°	366	24.6
9.4°	222	19.2
50.6°	222	19.2
52.7°	366	24.6
56.5°	1626	51.8

We show the performance of the KC^{S-S}_{Mo-Mo} to describe relaxation in the MSL (Fig. S4 and S5). Furthermore, the band structure for 7.3° and 52.7° tBLM obtained using the DFT

relaxed structure is compared to that obtained using SW+KC^{S-S}_{Mo-Mo} relaxed structure (Fig. S6).

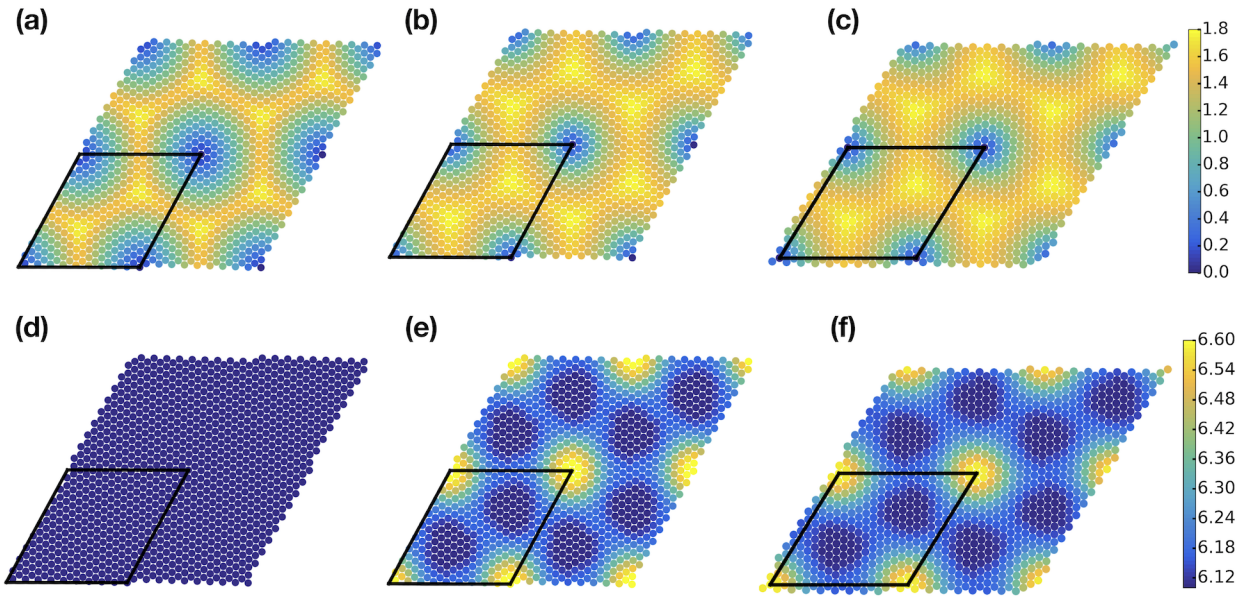

Figure S4: Distribution of interlayer spacings (ILS) and order-parameter (OP) in the MSL. (a) and (d) OP and ILS distribution in the rigidly-twisted bilayer MoS_2. The twist angle here is 3.5°. (b) and (e) ((c) and (f)) Distribution of OP and ILS in the MSL relaxed using using DFT (SW+KC^{S-S}_{Mo-Mo}), respectively.

4 Taper function

A taper function[S2–S5] can be multiplied to the the KC potential to make sure that the potential, its first and second derivatives go to zero at r_{cut}.

$$\begin{aligned} T(r_{ij}) =& 20(r_{ij}/r_{cut})^7 - 70(r_{ij}/r_{cut})^6 + 84(r_{ij}/r_{cut})^5 \\ & - 35(r_{ij}/r_{cut})^4 + 1 \end{aligned} \tag{1}$$

Note that the taper function affects the potential in the entire range of $0 < r_{ij} < r_{cut}$. To include the effect of taper, the KC parameters need to be refit. The refit KC^{X-X}_{M-M} interaction parameters are provided in Table S5. The shear mode and layer breathing mode frequencies

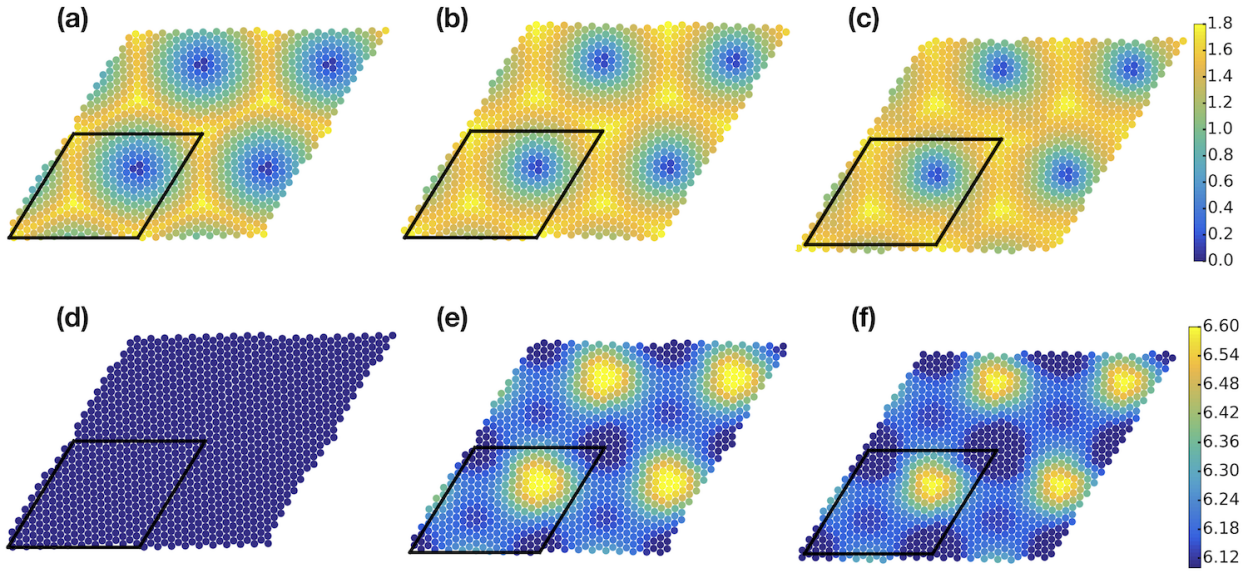

Figure S5: Distribution of interlayer spacings (ILS) and order-parameter (OP) in the MSL. (a) and (d) OP and ILS distribution in the rigidly-twisted bilayer MoS_2. The twist angle here is 56.5°. (b) and (e) ((c) and (f)) Distribution of OP and ILS in the MSL relaxed using DFT (SW+KC^{S-S}_{Mo-Mo}), respectively.

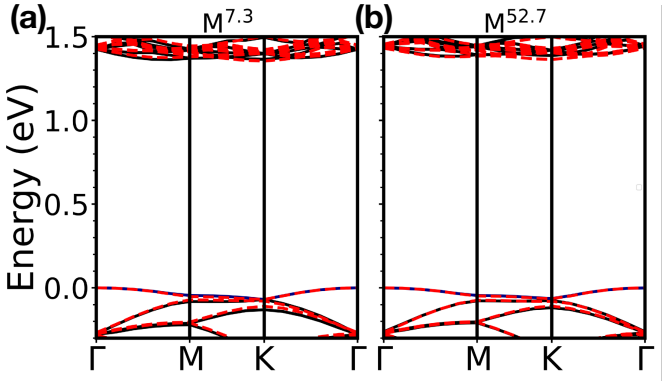

Figure S6: (a) and (b) Band structure of 7.3° and 52.7° twisted bilayer MoS_2, respectively Solid lines represent band structure computed using the DFT relaxed structure. Dashed lines represent the band structure computed using the forcefield (SW+KC^{S-S}_{Mo-Mo}) relaxed structure. The inset shows an enlarged plot of the valence bands. The flat band is marked in blue.

are compared with experimental measurements in Table S6. Fig. S7 compares BE computed using SW+KC^{X-X}_{M-M} (along with taper) with DFT calculations for MoS_2 and WSe_2. Fig. S8 similarly shows the performance of the mixing rule with these parameters for $MoS_2/MoSe_2$ and MoS_2/WS_2 heterostructures.

Table S5: Parameters for KC^{X-X}_{M-M} interaction with the taper function.

	z_0 (Å)	C_0 (meV)	C_2 (meV)	C_4 (meV)	C (meV)	δ (Å)	λ ($Å^{-1}$)	A (meV)
S_2-S_3	3.797	11.514	4.277	0.028	39.423	1.311	2.718	94.667
Se_2-Se_3	3.962	13.360	10.685	0.000	45.530	1.228	2.594	104.360
Mo_1-Mo_2	9.185	5.401	4.272	0.374	7.128	1.307	0.961	14.683
W_1-W_2	9.086	4.187	3.312	0.289	5.524	1.238	1.000	11.381

Table S6: Comparison of the shear (SM) and layer breathing modes (LBM) of bilayer TMDs computed using SW+KC^{X-X}_{M-M} (in presence of the taper function) with experimental measurements.

	LBM (cm^{-1})		SM (cm^{-1})	
	SW+KC^{X-X}_{M-M}	Expt.	SW+KC^{X-X}_{M-M}	Expt.
$BLMoS_2$	41.1	40,[S6] 41.6[S7]	24.8	22,[S6] 24.2[S7]
$BLWS_2$	32.9	33.8[S7]	20	19.6[S7]
$BLMoSe_2$	33.2	34.3,[S7] 29[S8]	21.6	21,[S7] 18[S8]
$BLWSe_2$	29.1	29.1,[S7] 27[S8]	18.0	17.7,[S7] 17[S8]

References

[S1] `http://www.physics.iisc.ernet.in/~mjain/pages/software.html`.

[S2] Leven, I.; Maaravi, T.; Azuri, I.; Kronik, L.; Hod, O. Interlayer Potential for Graphene/h-BN Heterostructures. *Journal of Chemical Theory and Computation* **2016**, *12*, 2896–2905.

[S3] Leven, I.; Azuri, I.; Kronik, L.; Hod, O. Inter-layer potential for hexagonal boron nitride. *The Journal of Chemical Physics* **2014**, *140*, 104106.

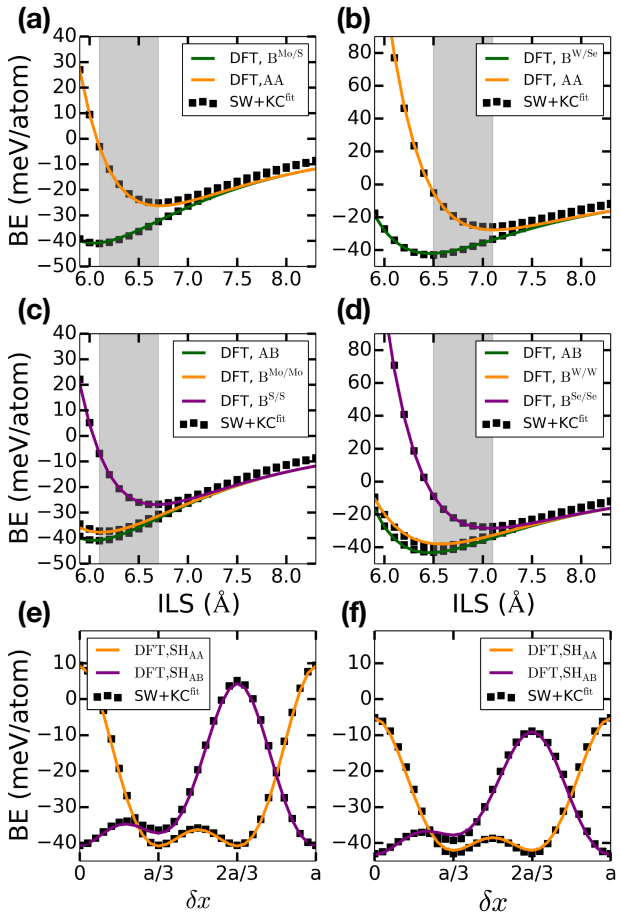

Figure S7: (a) and (c) ((b) and (d)) BE computed within DFT and using SW+$\mathrm{KC}^{\mathrm{X-X}}_{\mathrm{M-M}}$ (with taper) as a function of interlayer spacing (ILS) for the high-symmetry stackings in bilayer MoS_2 (WSe_2). The shaded region marks the range of possible interlayer spacings in the bilayer system. (e) ((f)) BE computed within DFT and using SW+$\mathrm{KC}^{\mathrm{X-X}}_{\mathrm{M-M}}$ (with taper) as a function of shear, SH_{AA} and SH_{AB}, in bilayer MoS_2 (WSe_2). The ILS here is fixed to that of the minimum ILS among the high-symmetry stackings.

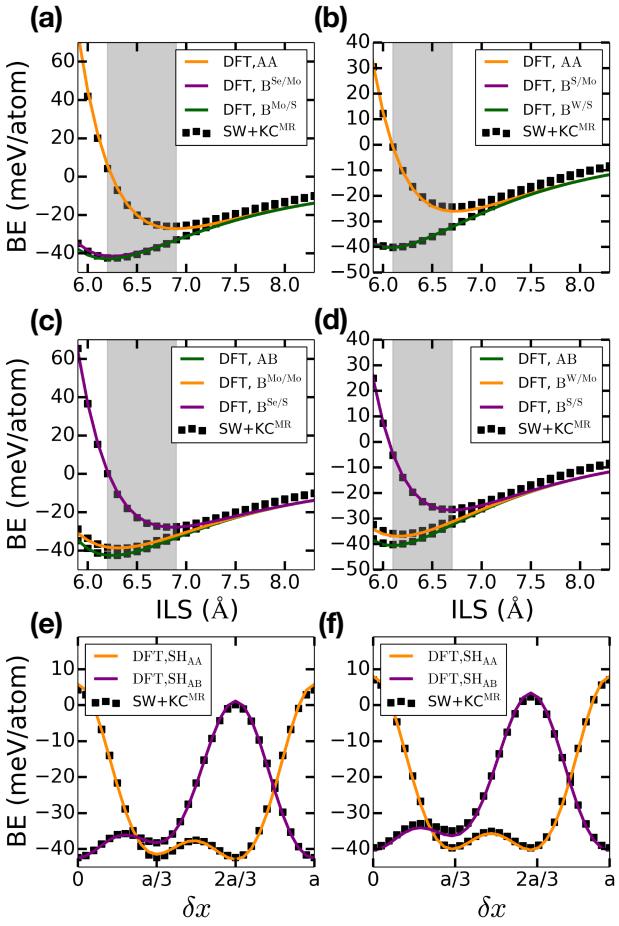

Figure S8: (a) and (c) ((b) and (d)) BE computed within DFT and using SW+KC^{X-X}_{M-M} (with taper) as a function of interlayer spacing (ILS) for the high-symmetry stackings in the heterostructure $MoS_2/MoSe_2$ (MoS_2/WS_2). The shaded region marks the range of possible interlayer spacings in the heterostructure system. (e) ((f)) BE computed within DFT and using SW+KC^{X-X}_{M-M} (with taper) as a function of shear, SH_{AA} and SH_{AB}, in the heterostructure $MoS_2/MoSe_2$ (MoS_2/WS_2). The ILS here is fixed to that of the minimum ILS among the high-symmetry stackings.

[S4] Wen, M.; Carr, S.; Fang, S.; Kaxiras, E.; Tadmor, E. B. Dihedral-angle-corrected registry-dependent interlayer potential for multilayer graphene structures. *Phys. Rev. B* **2018**, *98*, 235404.

[S5] Ouyang, W.; Mandelli, D.; Urbakh, M.; Hod, O. Nanoserpents: Graphene Nanoribbon Motion on Two-Dimensional Hexagonal Materials. *Nano Letters* **2018**, *18*, 6009–6016.

[S6] Zhao, Y.; Luo, X.; Li, H.; Zhang, J.; Araujo, P. T.; Gan, C. K.; Wu, J.; Zhang, H.; Quek, S. Y.; Dresselhaus, M. S.; Xiong, Q. Interlayer Breathing and Shear Modes in Few-Trilayer MoS2 and WSe2. *Nano Letters* **2013**, *13*, 1007–1015.

[S7] Chen, S.-Y.; Zheng, C.; Fuhrer, M. S.; Yan, J. Helicity-Resolved Raman Scattering of MoS2, MoSe2, WS2, and WSe2 Atomic Layers. *Nano Letters* **2015**, *15*, 2526–2532.

[S8] O"Brien, M.; McEvoy, N.; Hanlon, D.; Hallam, T.; Coleman, J. N.; Duesberg, G. S. Mapping of low-frequency raman modes in cvd-grown transition metal dichalcogenides: Layer number, stacking orientation and resonant effects. *Scientific reports* **2016**, *6*, 19476.